



ARTICLE

Numerical Study of Multi-Factor Coupling Effects on Energy Conversion Performance of Nanofluidic Reverse Electrodialysis

Hao Li¹, Cunlu Zhao², Jinhui Zhou¹, Jun Zhang³, Hui Wang¹, Yanmei Jiao^{1,*} and Yugang Zhao^{4,5,*}

¹School of Physical and Mathematical Sciences, Nanjing Tech University, Nanjing, 211816, China

²MOE Key Laboratory of Thermo-Fluid Science and Engineering, Xi'an Jiaotong University, Xi'an, 710049, China

³Key Laboratory of Unsteady Aerodynamics and Flow Control, Ministry of Industry and Information Technology, Nanjing University of Aeronautics and Astronautics, Nanjing, 210016, China

⁴Shanghai Key Laboratory of Multiphase Flow and Heat Transfer in Power Engineering, School of Energy and Power Engineering, University of Shanghai for Science and Technology, Shanghai, 200093, China

⁵Key Laboratory of Icing and Anti/De-icing, China Aerodynamics Research and Development Center, Mianyang, 621000, China

*Corresponding Authors: Yanmei Jiao. Email: jiaoym@njtech.edu.cn; Yugang Zhao. Email: ygzhao@usst.edu.cn

Received: 12 January 2025; Accepted: 28 February 2025; Published: 25 April 2025

ABSTRACT: Based on the rapid advancements in nanomaterials and nanotechnology, the Nanofluidic Reverse Electrodialysis (NRED) has attracted significant attention as an innovative and promising energy conversion strategy for extracting sustainable and clean energy from the salinity gradient energy. However, the scarcity of research investigating the intricate multi-factor coupling effects on the energy conversion performance, especially the trade-offs between ion selectivity and mass transfer in nanochannels, of NRED poses a great challenge to achieving breakthroughs in energy conversion processes. This numerical study innovatively investigates the multi-factor coupling effect of three critical operational factors, including the nanochannel configuration, the temperature field, and the concentration difference, on the energy conversion processes of NRED. In this work, a dimensionless amplitude parameter s is introduced to emulate the randomly varied wall configuration of nanochannels that inherently occur in practical applications, thereby enhancing the realism and applicability of our analysis. Numerical results reveal that the application of a temperature gradient, which is oriented in opposition to the concentration gradient, enhances the ion transportation and selectivity simultaneously, leading to an enhancement in both output power and energy conversion efficiency. Additionally, the increased fluctuation of the nanochannel wall from $s = 0$ to $s = 0.08$ improves ion selectivity yet raises ion transport resistance, resulting in an enhancement in output power and energy conversion efficiency but a slight reduction in current. Furthermore, with increasing the concentration ratio c_H/c_L from 10 to 1000, either within a fixed temperature field or at a constant dimensionless amplitude, the maximum power consistently attains its optimal value at a concentration ratio of 100 but the cation transfer number experiences a monotonic decrease across this entire range of concentration ratios. Finally, upon modifying the operational parameters from the baseline condition of $s = 0$, $c_H/c_L = 10$, and $\Delta T = 0$ K to the targeted condition of $s = 0.08$, $c_H/c_L = 50$, and $\Delta T = 25$ K, there is a concerted improvement observed in the open-circuit potential, short-circuit current, and maximum power, with respective increments of 8.86%, 204.97%, and 232.01%, but a reduction in cation transfer number with a notable decrease of 15.37%.

KEYWORDS: Salinity gradient energy; nanofluidic reverse electrodialysis; energy conversion; nanochannel configuration; multi-factor coupling effect



1 Introduction

Salinity Gradient Energy (SGE), a kind of Gibbs free energy that releases naturally from the mixing of solutions with different concentrations, holds immense potential for widespread utilization as a sustainable and eco-friendly energy source. Three prevalent energy conversion methodologies, namely Pressure Retarded Osmosis (PRO), Vapor Pressure Difference (VPD) Energy, and Reverse Electrodialysis (RED), have been extensively researched and implemented for the extraction of SGE [1]. In comparison to PRO and VPD, RED exhibits a significant advantage by directly transforming SGE into electricity solely through the utilization of ion-selective membranes. This approach circumvents the mechanical energy losses encountered in PRO and the heat dissipation associated with VPD, thereby rendering RED a highly efficient and often-termed osmotic energy conversion technique [2,3]. Recently, the rapid advancements in nanotechnology and innovative nanomaterials have ushered in a new era of enhanced RED, commonly known as Nanofluidic Reverse Electrodialysis (NRED) [4,5]. Instead of using conventional ion-selective membranes, this cutting-edge NRED system innovatively incorporates nanofluidic-enabled membranes, which exhibit exceptional capabilities in facilitating mass transfer, thereby propelling the energy conversion efficiency of the SGE to unprecedented heights.

Numerous experimental and numerical studies on the NRED have been carried out from different perspectives [6–11], such as nanochannel geometries [12–15], surface charge densities of nanochannels [16–18], nanochannel materials [19], solute concentrations [20,21], solution temperatures [22], pH values of solutions [23], and their effects on the energy conversion performance of the NRED system. It is found that the geometric configurations of nanochannels play a pivotal role in determining the energy conversion performance of the NRED system. Specifically, nanochannels with longer lengths and smaller diameters potentially give rise to high output power [24,25]. However, it is also demonstrated that maximal energy conversion efficiencies could only be achieved at certain optimal nanochannel lengths [26]. Asymmetric nanochannels, such as conical nanochannels [27], bullet-shaped nanochannels [28], asymmetric nano-roughness-featured nanochannels [29], etc., perform differently during the energy conversion processes when coupling with different concentration gradients. In practical applications, the radii of nanochannels often exhibit random variations along their length due to prevalent fabrication imperfections, resulting in an irregular geometry that can significantly impact their performance characteristics. In addition, it is noteworthy to mention that membranes employed in the majority of RED experiments can be equivalently regarded as a cluster of irregularly shaped nanochannels.

Concentration ratio between the two solutions to be mixed is another key parameter in determining the energy conversion performance of NRED. It has been observed that an increment in the concentration ratio, within a relatively low range, results in a corresponding enhancement of the generated potential [25]. However, a subsequent increase in the concentration ratio beyond a certain threshold adversely affects ion selectivity, resulting in a subsequent decline in the generated potential [23]. Thus, it is logically deduced that the potential initially escalates and subsequently decrease as the concentration ratio rises. However, contrasting findings from certain studies reveal a monotonic augmentation of potential with an increment in concentration ratio, which is also related to the nanochannel length [24].

Recent extensive researches have unveiled a pivotal role of solution temperature in governing the intricacies of energy conversion processes [30,31]. This critical parameter influences ion transportations [32,33], modulates currents [34,35], controls potentials and consequently impacts the overall energy conversion efficiency in a complicated manner [36–39]. In particular, asymmetric thermal environments have demonstrated remarkable capabilities in mitigating the ion concentration polarization (ICP) effect at the interface between nanopores and the reservoir, particularly within regions of low solution concentration. This mitigation subsequently enhances the corresponding energy conversion processes [40,41]. Another research

has also revealed that the utilization of a NRED device, when coupled with a photothermal condition, significantly enhances the efficiency of harvesting SGE [42]. Furthermore, leveraging temperature effects to enhance the performance of salinity gradient energy can facilitate the recovery and conversion of low-grade thermal energy [43,44]. Moreover, integrating salinity gradient energy with solar power generation can further enhance the efficiency of both energy sources [45,46].

Generally, the performance of the NRED system is intricately influenced by a series of complex factors. Although extensive research works have been carried out on NRED, the majority of them have predominantly focused on isolating and examining the influence of individual characteristics on energy conversion processes. The comprehensive investigations on complex interplay and coupling effects of multiple factors remain scarce. This study aims to examine the complicated multi-factor coupling effects of three pivotal parameters, including the nanochannel geometry, solution temperature, and the solution concentration, on the energy conversion processes of NRED. Particularly, axisymmetric nanochannels with randomly varying wall curvature are going to be innovatively considered. The core performance metrics, which encompass the open-circuit potential, short-circuit current, maximum power output, cation transfer number, and ultimately, the energy conversion efficiency across the nanochannels, will be systematically analyzed under various prescribed conditions.

2 Mathematical Model

2.1 Numerical Model

As depicted in a typical energy conversion system of NRED in Fig. 1a, an axisymmetric nanochannel, featured with varied radii along the axial direction, bridges two reservoirs at each end of the nanochannel. Two KCl solutions, with two different solution concentrations of c_H and c_L (where $c_H > c_L$) and two different solution temperatures of T_H and T_L , are filled in the reservoirs, respectively. Since the thermal conductivity across the nanochannel membrane is also considered in this study, the computational domain involves both the fluid and the solid components for mass and heat transfer. Fig. 1b illustrates the corresponding computational domain of the energy conversion system. The wall of the nanochannel, consisting of a randomly distributed curve, is controlled by a scaling factor of amplitude, s . When s equals 0, the wall of the nanochannel becomes a straight line and the radius of the nanochannel equals the mean radius, as indicated by the dashed line in green in the figure. When $s > 0$, the nanochannel wall deviates from a straight line and exhibits random variations. Notably, larger values of s lead to more significant variations in the amplitude of the nanochannel wall. In addition, the gradient direction of the temperature that is opposite to that of the concentration is defined as the negative temperature gradient in this study.

The steady-state Poisson-Nernst-Planck equation integrated with the Navier-Stokes equation are employed to simulate ion transports in nanochannels where the temperature and concentration gradients exists [21,41]. To facilitate numerical calculations and comparisons, a set of characteristic parameters are defined for scaling the governing equations: length $L_{ref} = a$; concentration $c_{ref} = c_0$ with c_0 representing the low solution concentration; temperature $T_{ref} = T_0$; relative permittivity $\epsilon_{r,ref} = \epsilon_{r,0}$ with $\epsilon_{r,0}$ representing the dielectric constant at $T = T_0$; diffusion coefficient $D_{1,ref} = D_{1,0}$, $D_{2,ref} = D_{2,0}$ with $D_{1,0}$ and $D_{2,0}$ respectively representing diffusion coefficients of cations and anions at $T = T_0$; potential $\phi_{ref} = RT_{ref}/F$ with R and F respectively representing the Universal gas constant and the Faraday constant; electric strength $E_{ref} = \phi_{ref}/L_{ref}$; fluid viscosity $\mu_{ref} = \mu_0$; charge density $\sigma_{ref} = \epsilon_0 \epsilon_{r,ref} \phi_{ref}/L_{ref}$ with ϵ_0 representing the vacuum dielectric constant; velocity $u_{ref} = (\epsilon_0 \epsilon_{r,ref} \phi_{ref}/L_{ref})E_{ref}$; pressure $p_{ref} = \mu_{ref} (u_{ref}/L_{ref})$; electric current density $i_{ref} = F u_{ref} c_{ref}$; electric conductivity $\tau_{ref} = i_{ref} L_{ref}/\phi_{ref}$. In addition, dimensionless numbers are defined as Reynolds number $Re = \rho u_{ref} L_{ref}/\mu_{ref}$ with ρ representing the fluid density, Peclet number of cation $Pe_1 = u_{ref} L_{ref}/D_1$ with D_1 representing the diffusion coefficient of the cation K^+ , Peclet number of anion $Pe_2 = u_{ref}$

L_{ref}/D_2 with D_2 representing the diffusion coefficient of the anion Cl^- , and $\text{Pe}_T = \rho u_{ref} L_{ref} C_p/k$ with C_p and k respectively representing the specific capacity and thermal conductivity. Consequently, the dimensionless form of the governing equations is achieved as follows [27,47–50]:

$$\tilde{\nabla} \tilde{\phi} = -\frac{1}{2} \lambda^2 \sum z_k \tilde{c}_k \quad (1)$$

$$\tilde{\nabla} \tilde{u} = 0 \quad (2)$$

$$\tilde{\nabla} \tilde{c}_k u \tilde{D}_k / \text{Pe}_k \left(\tilde{\nabla}^2 \tilde{c}_k + z_k \tilde{\nabla} \tilde{c}_k \tilde{\nabla} \tilde{\phi} + 2\alpha_k \tilde{\nabla} \tilde{c}_k \tilde{\nabla} \tilde{T} / T \right) = 0 \quad (3)$$

$$\text{Re}(\tilde{u} \tilde{\nabla} \tilde{u}) = -\tilde{\nabla} \tilde{p} + \tilde{\mu} \tilde{\nabla}^2 \tilde{u} - \frac{1}{2} \tilde{\nabla} \tilde{\phi} \sum z_k \tilde{c}_k - \frac{1}{2} |-\tilde{\nabla} \tilde{\phi}|^2 \tilde{\nabla} \tilde{\epsilon}_r = 0 \quad (4)$$

$$\text{Pe}_T \tilde{u} \tilde{\nabla} \tilde{T} = \tilde{\nabla}^2 \tilde{T} \quad (5)$$

where the subscript k is denoted as 1 or 2, representing ionic specie K^+ or Cl^- , respectively. In addition, z_k is the valence of the ionic specie, λ is the scaled Debye length, expressed as $\lambda = \left[(2c_0 F_2 a^2) / (\epsilon_0 \epsilon_r R T_0) \right]^{1/2}$, α_k is the reduced Soret coefficient. Then the electric current density is additionally given as:

$$\tilde{i} = \tilde{u} \sum z_k \tilde{c}_k - \sum \tilde{D}_k / \text{Pe}_k \left(z_k \tilde{\nabla} \tilde{c}_k + z_k^2 \tilde{c}_k \tilde{\nabla} \tilde{\phi} + 2z_k \alpha_k \tilde{c}_k \tilde{\nabla} \tilde{T} / T \right) \quad (6)$$

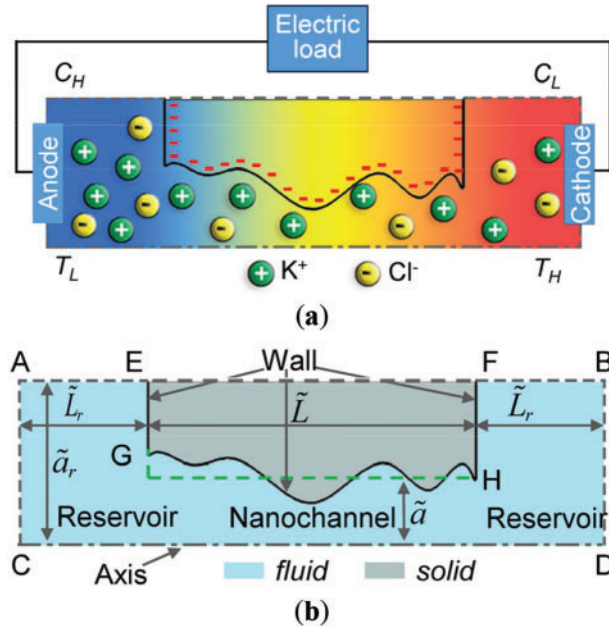


Figure 1: Schematic of a typical energy conversion system of NRED. (a) An energy conversion system of NRED within an electric circuit. (b) The corresponding calculation domain for the numerical study

Remarkably, some certain parameters cannot be considered as constants within a calculation domain where the temperature gradient exists. They should be expressed as functions of the temperature [30,42]:

$$\epsilon_r = \exp \left(4.4716 - 4.60128 \times 10^{-3} dT + 2.6952 \times 10^{-7} dT^2 \right) \quad (7)$$

where $dT = T - 273.15$, $0 < dT < 100$.

$$\mu = 2.414 \times 10^{-5} \times 10^{247.8/(T-140)} \quad (8)$$

where $273.15 \leq T \leq 643.15$.

$$D_i = \frac{RT}{F^2} \left[\frac{1/|z_k|}{1/\tau_{m,k}^0} \right] \tag{9}$$

where $\tau_{m,k}^0$ is the limiting molar conductivity of the i th ionic specie. In particular, $\tau_{m,1}^0 = 40.5017 + 1.2194(dT) + 4.1859 \times 10^{-3}(dT)^2$ and $\tau_{m,2}^0 = 76.35 + 1.51037(\delta T) + 4.65 \times 10^{-3}(\delta T)^2 - 1.285 \times 10^{-5}(\delta T)^3$. δT is the temperature difference of the heat source compared to the reference temperature of 298 K (i.e., $\delta T = T - 298$). The following performance parameters of the energy conversion process of the NRED are thoroughly investigated in this work, including the open-circuit potential $\tilde{\phi}_{oc}$, short-circuit current \tilde{I}_{sc} , power \tilde{P} , maximum power $\tilde{P}_{max} = \tilde{\phi}_{oc}\tilde{I}_{sc}/4$, cation transfer number $t_+ = \tilde{I}_+ / (\tilde{I}_+ + |\tilde{I}_-|)$, and maximum energy conversion efficiency $\eta_{max} = (2t_+ - 1)^2/2$.

2.2 Boundary Conditions

Different boundary conditions are used to achieve the open-circuit potential $\tilde{\phi}_{oc}$, short-circuit current \tilde{I}_{sc} , as well as the potential-current ($\tilde{\phi} - \tilde{I}$) curve. As depicted in Fig. 1b, the potential at the boundary AC is always set as zero, When the current at the boundary BD, expressed as $\int_A \tilde{i}$ as shown in Table 1, is set as zero, the induced at this boundary is precisely the open-circuit potential $\tilde{\phi}_{oc}$. In contrast, when the potential at the boundary BD is set as zero, the induced current is precisely the short-circuit current \tilde{I}_{sc} . The corresponding $\tilde{\phi} - \tilde{I}$ curve can be consequently obtained by setting the potential at the boundary BD as $\tilde{\phi} = \tilde{\phi}_0$ ($0 < \tilde{\phi}_0 < \tilde{\phi}_{oc}$). All the other relevant boundary conditions are elaborated in Table 1.

Table 1: Boundary conditions set for the 2D axisymmetric calculation domain applied in this study. $\tilde{\sigma}$ is the surface charge density

Boundary	Electric field	Ion transport	Flow field	Heat transfer
AC	$\tilde{\phi} = 0$	\tilde{c}_H	$P = 0$	T_L
AE, FB	$\nabla \tilde{\phi} = 0$	No flux	Slip	Thermal insulation
EG, FH	$\frac{\partial \tilde{\phi}}{\partial \tilde{r}} = -\tilde{\sigma}$	No flux	No slip	Thermal insulation
GH	$\frac{\partial \tilde{\phi}}{\partial \tilde{r}} = -\tilde{\sigma}$	No flux	No slip	$T_f = T_s$
BD	$\int_A \tilde{i} = 0$	1	$P = 0$	T_H
CD	Axis of symmetry	Axis of symmetry	Axis of symmetry	Axis of symmetry
EF	/	/	/	Thermal insulation

3 Results and Discussion

3.1 Model Validation

A research work reported by Mai et al. [41] is reproduced and compared in this work to validate the proposed theoretical and numerical model. A comprehensive investigation was conducted on a nanochannel, with a focus on its energy conversion behavior under the intricate interplay of temperature and concentration gradients. The radii, length, and surface charge density of the nanochannel were given as 5, 1000 nm, and $-5 \text{ mC}\cdot\text{m}^{-2}$, respectively. At one end of the nanochannel, the KCl solution was adjusted to a precise concentration of 1 mM, whereas at the opposite end, the concentration was varied systematically, spanning from 1 to 1000 mM, respectively. In addition, on the side with the higher concentration of KCl, the

temperature was precisely set at 298 K, whereas on the side featuring a lower concentration, the temperature was adjusted to 323 K, respectively. As illustrated in Fig. 2, the induced potential achieved based on the numerical model applied in this work is compared with the ones numerically and experimentally obtained in literature [41]. The remarkable consistent results validate the feasibility and reliability of the theoretical and numerical model proposed in this study for accurately capturing mass transfer phenomena in nanochannels under conditions of the concentration and temperature gradients.

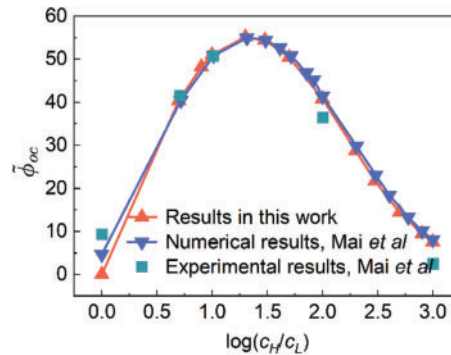


Figure 2: Validation of the theoretical and numerical model proposed in this work

3.2 Osmotic Energy Conversion

As depicted in Fig. 1b, the dimensionless sizes of the nanochannel and the reservoirs are $\tilde{a} \times \tilde{L} = 1 \times 50$ and $\tilde{a}_r \times \tilde{L}_r = 50 \times 50$, respectively. Taking the room temperature of $T_0 = 298$ K as the baseline temperature, then the relevant physical parameters at this temperature are given as follows: $\mu_0 = 8.9 \times 10^{-4}$ Pa·s, $D_{1,0} = 1.957 \times 10^{-9}$ m²/s, $D_{2,0} = 2.032 \times 10^{-9}$ m²/s, $\epsilon_{r,0} = 78$. The characteristic length and the characteristic concentration are set as $a = 10$ nm and $c_0 = 1$ mM, respectively. In addition, the reduced Soret coefficient and constants are $\alpha_{1(K^+)} = 0.5$, $\alpha_{2(Cl^-)} = 0.1$ [21], $F = 9.649 \times 10^4$ C·mol⁻¹, $R = 8.314$ J·K⁻¹·mol⁻¹ and $\epsilon_0 = 8.854 \times 10^{-12}$. Then the corresponding characteristic groups are calculated as $\phi_{ref} = 2.57 \times 10^{-2}$ V, $u_{ref} = 4.56 \times 10^{-2}$ m·s⁻¹, $p_{ref} = 4.56 \times 10^3$ Pa, $\sigma_{ref} = 1.77$ mC·m⁻². The numerical model was solved by a finite-element analysis software, COMSOL Multiphysics 6.1, and free triangular meshes were employed in this work. The grid independence test was conducted first. Variations of the open-circuit potential and the short-circuit current with the increment of the number of meshes are drawn in Fig. 3. It is found that the discretization strategy with a total grid number of 26,473 gives rise to relatively stable potential and current when comparing with the other discretization strategies. Therefore, all the following parametric numerical calculations were carried out based on this discretization strategy.

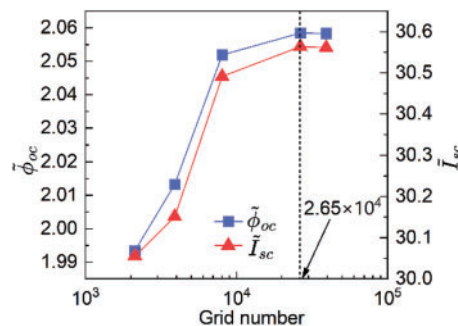


Figure 3: Grid independence test

3.2.1 Effect of Temperature

The general effects of temperature on the osmotic energy conversion happening at given conditions of $c_H/c_L = 50$, nanochannel of $s = 0.06$ are investigated first. As shown in Fig. 4a, four different temperature fields are imposed on the energy conversion system: (I) uniform temperature of 298 K across the nanochannel denoted as T -298 K, (II) uniform temperature of 323 K across the nanochannel denoted as T -323 K, (III) temperature field with temperatures of 298 and 323 K respectively at the left (high-concentration side) and right (low-concentration side) terminals denoted as T -298 K/323 K, (IV) temperature field with temperatures of 323 and 298 K respectively at the left (high-concentration side) and right (low-concentration side) terminals denoted as T -323 K/298 K. In this study, the low-concentration solution is always fixed as 1 at the right terminal of the NRED system and the high-concentration solution is placed at the left side. Therefore, the temperature gradient that has the same direction as that of the concentration gradient is defined as the positive temperature gradient. Otherwise, the temperature gradient that is opposite to the concentration gradient is defined as the negative temperature gradient. Fig. 4b presents variations of the current and the output power with the potential at these four different temperature fields. Generally, linear variations of the current with the potential are observed for all four temperature fields. Thus, the corresponding maximum power occurs at the half of the open-circuit potential, given as $\tilde{P}_{max} = \tilde{\phi}_{oc}\tilde{I}_{sc}/4$. It is observed from Fig. 4b,c that the isothermal scenario of T -323 K yields the highest open-circuit potential, short-circuit current, and power, while the isothermal scenario of T -298 K yields the lowest performance of these three parameters. Both the scenarios of T -298 K/323 K and T -323 K/298 K, which exhibit non-uniform temperature distributions yet maintain an identical average temperature, give rise to intermediate results compared to the two isothermal scenarios as mentioned above and, meanwhile, they perform closely with each other. It reasonably proves that high solution temperatures are beneficial to inducing better performance in aspects of the open-circuit potential, short-circuit current, as well as the output power. However, remarkable different variation trend of the effect of the temperature on the cation transfer number t_+ is observed in Fig. 4c where the scenarios of T -323 K and T -298 K/323 K yields the lowest and the highest cation transfer numbers, respectively. This special trend will be thoroughly explored in cooperation with all kinds of ion flow rate investigated in the following section. Consequently, based on the theoretical equation $\eta_{max} = (2t_+ - 1)^2/2$, it is logically deduced that these temperature conditions of T -323 K and T -298 K/323 K correspondingly result in the lowest and the highest maximum conversion efficiencies. Generally, the Fig. 4 shows that although the high average temperature of a solution can yield better output power, it leads to low energy conversion efficiency. On the contrary, the scenario of T -298 K/323 K gives rise to lowest output power but the highest energy conversion efficiency.

All these variations trends above are dominated by ion transportations within the nanochannel which are essentially reflected by the induced currents. As theoretically presented by Eq. (6), current density throughout the nanochannel is simultaneously dominated by mechanisms of convection, diffusion, migration, and thermophoresis, which jointly forms the overall electric current of the NRED system. Since the current density under the short-circuit condition reaches the maximum value and thus can reflect effects of each factor more distinctly. Therefore, as shown in Fig. 5, the contour plot of the current density at the short-circuit scenario and the corresponding current, defined as the surface integration of the current density distributed at a certain cross-section area, varying along the axial direction under conditions of T -298 K/323 K, $s = 0.06$, and $c_H/c_L = 50$, are investigated first. It is found that although the overall current is a constant at around a dimensionless value of 13 throughout the nanochannel, the corresponding variations of each current components along the axial direction are remarkably different with each other. As a result of the selectivity and rectification characteristics of the nanochannel, the ion concentration polarization phenomenon becomes more pronounced [50], particularly at the interface between the nanochannel and its

attached reservoirs. Consequently, the diffusion current and migration current undergo notable fluctuations along the axial direction, with peak variations observed at the junction region. In contrast, the convection current and thermophoresis current remain relatively modest and stable throughout. Importantly, the overall current is mainly dominated by the diffusion current and migration current. Furthermore, it is also noticed that the thermophoresis current varies moderately from -800 at the left junction to 0 at the right junction.

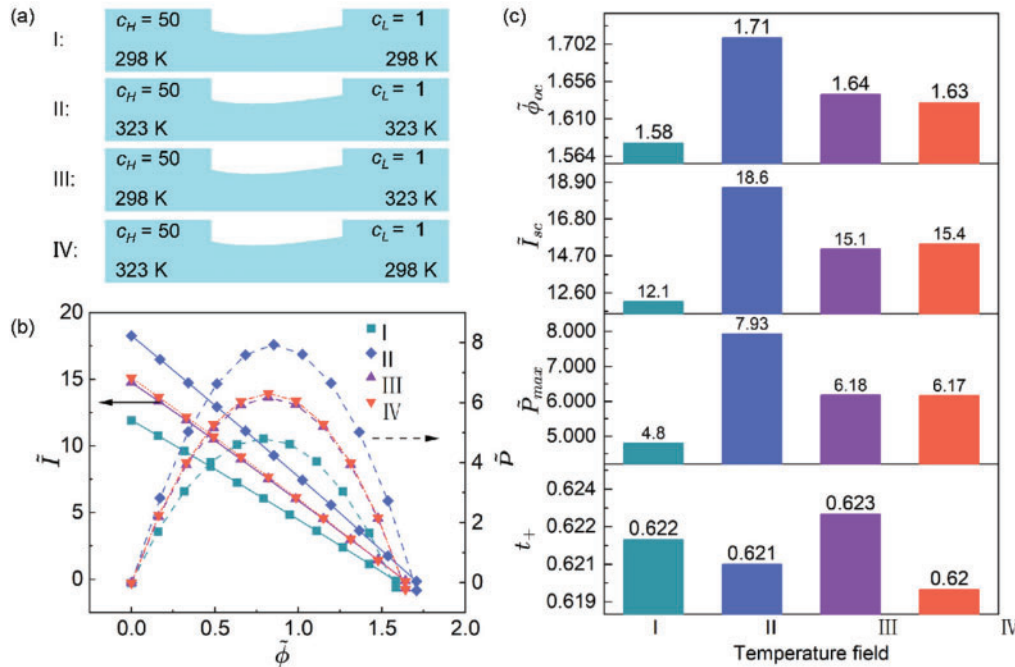


Figure 4: Effects of temperature on the osmotic energy conversion under given conditions of $s = 0.06$ and $c_H/c_L = 50$. (a) Four temperature fields imposed on nanochannel-based the energy conversion system. (b) Variations of the current and the corresponding output power with the potential. (c) Open-circuit potentials, short-circuit currents, maximum powers, and the corresponding cation transfer numbers achieved at these four different temperature fields

The solution temperature significantly influences the transportations of different ion species during the energy conversion process at different levels. Variations of the cation and anion flow rates and the corresponding currents along the axis of the middle region of the nanochannel under conditions of $s = 0.06$, $c_H/c_L = 50$ are summarized in Fig. 6. Fig. 6a–c shows that isothermal scenarios of $T=323$ K and $T=298$ K yield the highest and lowest anion/cation flow rates, respectively. The scenarios of $T=323$ K/298 K and $T=298$ K/323 K exhibit intermediate effects on the ion flow rates compared to these two isothermal scenarios. In addition, since the ion flow rate induced by thermophoresis is directly related with the temperature, it varies remarkably different with the convection, diffusion, and migration ion flow rates when the temperature field changes within the nanochannel. As for the scenario of $T=323$ K/298 K, since the temperature gradient has the same direction with the concentration gradient, the direction of the induced thermophoresis ion flow rate is from the high-concentration side to the low-concentration side. Therefore, the scenario of $T=323$ K/298 K enhance the ion flow rate. Opposite influences occur at the scenario of $T=298$ K/323 K which eventually weakens the ion flow rate. The isothermal scenarios of $T=323$ K and $T=298$ K have negligible impact on the ion flow rate since there is no temperature gradient within the nanochannel. The overall current is thus achieved according to the relationship of $\tilde{I}_{overall} = \tilde{q}_{+,overall} \cdot z_1 + \tilde{q}_{-,overall} \cdot z_2$, the variation trends of which along the axial direction are similar with those of the cation/anion flow rate.

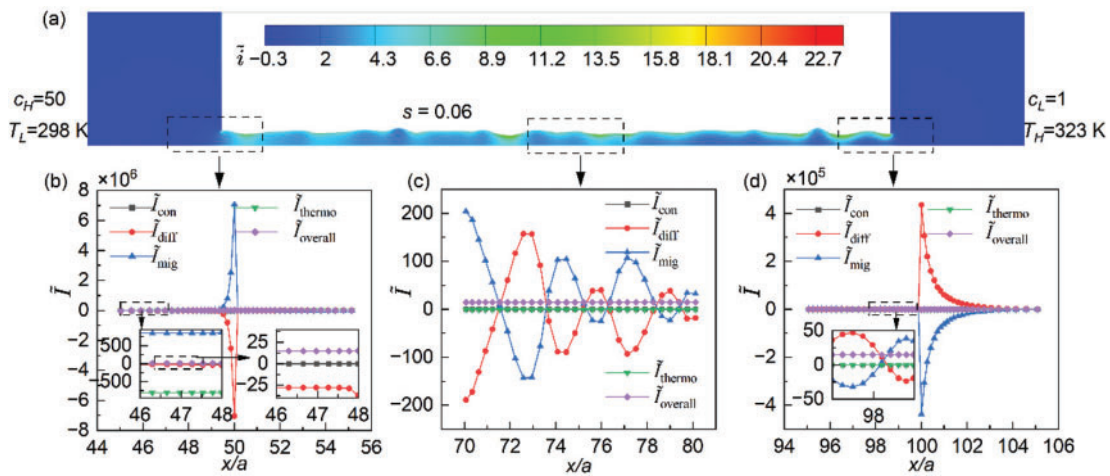


Figure 5: Contour plot of current density and variations of the overall current and its components along the axial direction of the nanochannel at the short-circuit scenario under conditions of $T=298\text{ K}/323\text{ K}$, $s = 0.06$, and $c_H/c_L = 50$: (a) Contour plot of the overall current density at the short-circuit scenario, (b) Variation of the overall current and each current component at the left junction of the channel, (c) Variation of the overall current and each current component at the middle section of the channel, (d) Variation of the overall current and each current component at the right junction of the channel

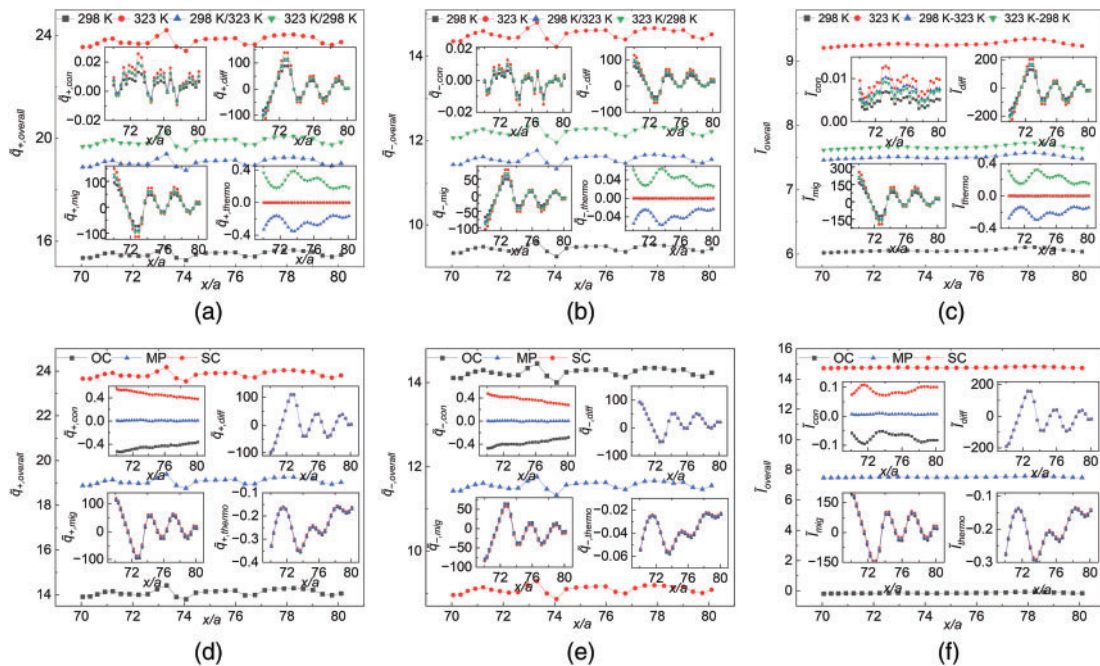


Figure 6: Variations of the ion flow rates and the corresponding currents along the axis of the middle region of the nanochannel at different scenarios: (a) Cation flow rate achieved at scenario of \dot{P}_{max} , (b) Anion flow rate achieved at scenario of \dot{P}_{max} , (c) Current achieved at scenario of \dot{P}_{max} , (d) Cation flow rate achieved at scenario of $T=298\text{ K}/323\text{ K}$, (e) Anion flow rate achieved at scenario of $T=298\text{ K}/323\text{ K}$, (f) Current achieved at scenario of $T=298\text{ K}/323\text{ K}$. The other related operation parameters of the NRED system are given as $s = 0.06$ and $c_H/c_L = 50$

Taking the scenario of $T=298\text{ K}/323\text{ K}$ as an example, variations of ion flow rates and the corresponding currents along the axis of the middle region of the nanochannel are compared in Fig. 6d–f. The variations of

all the flow rates contributed by different mechanisms, as shown in Fig. 6d,e, prove that ion transportations within the nanochannel is dominated by mechanisms of the diffusion and the migration. Therefore, as for a NRED system operating under certain concentration and temperature gradients, the ion transportations are only affected by migration for all electric circuit states. Consequently, the cation and anion flow rates only vary with the induced potential of the energy conversion system. As for the open-circuit situation, since the induced potential reaches the maximum, the cation and the anion flow rates reach the maximum and the minimum values, respectively. On the contrary, the cation flow rate and the anion flow rate reach the minimum and the maximum values, respectively, under the short-circuit condition where the induced potential is zero. Finally, the overall currents under the open-circuit, the maximum power, and the short-circuit conditions are estimated at around 0, 7.53, and 14.77, respectively.

As shown in Fig. 4c, the cation transfer number t_+ is observed to vary oppositely with the other performance parameters under different temperature fields. Since the energy conversion efficiency, one of the most essential energy conversion parameters, is only a function of the cation transfer number t_+ , it is necessary to make clear why the cation transfer number varies so differently. The cation transfer number t_+ is calculated as $t_+ = \tilde{I}_+ / (\tilde{I}_+ + |\tilde{I}_-|)$, where $\tilde{I}_+ = \tilde{q}_{+,overall} \cdot z_1$ and $\tilde{I}_- = \tilde{q}_{-,overall} \cdot z_2$. Since z_1 and z_2 respectively are 1 and -1 in this work, the cation transfer number thus can be expressed as a function of ion flow rates, that is $t_+ = \tilde{q}_{+,overall} / (\tilde{q}_{+,overall} + \tilde{q}_{-,overall})$. According to calculations, although the cation transfer number fluctuates along the axial direction of the NRED system, it stabilizes at a certain average value throughout the NRED system and it is almost a constant within the reservoir region. Therefore, at the given scenario of the maximum power, $s = 0.06$, and $c_H/c_L = 50$, variations of ion flow rates and the corresponding cation transfer numbers with the temperature gradient, obtained at the right terminal of the reservoir, are investigated as shown in Fig. 7.

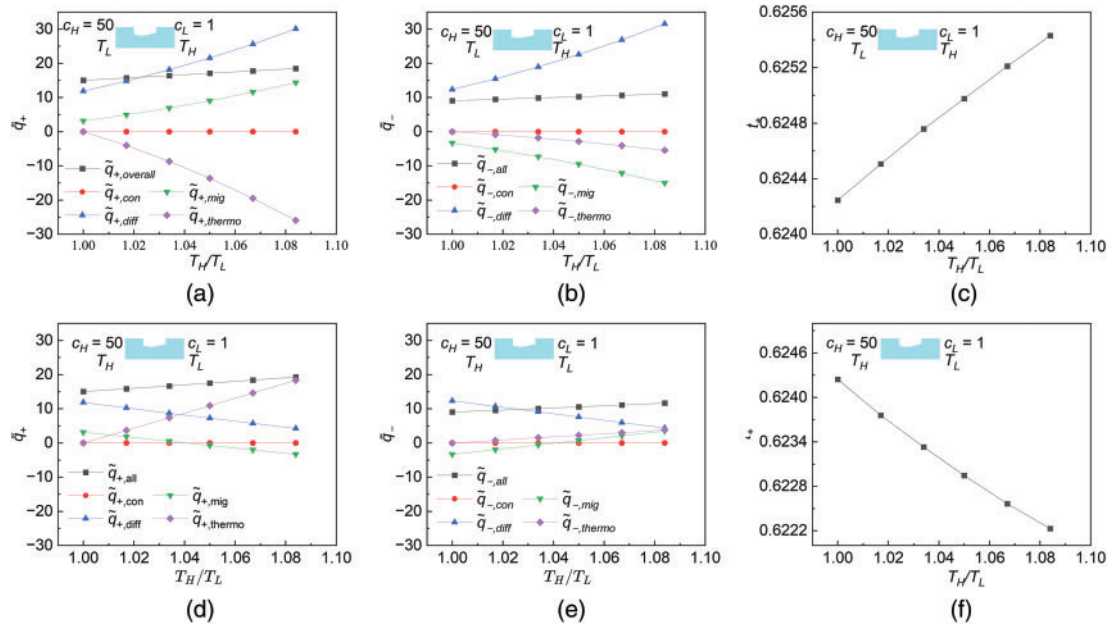


Figure 7: Variations of ion flow rates and the corresponding cation transfer numbers with the temperature gradient at the scenario of the maximum power, $s = 0.06$, and $c_H/c_L = 50$. (a) Cation flow rate under the negative temperature gradient, (b) Anion flow rate under the negative temperature gradient, (c) Cation transfer number under the negative temperature gradient, (d) Cation flow rate under the positive temperature gradient, (e) Anion flow rate under the positive temperature gradient, (f) Cation transfer number under the positive temperature gradient

When a negative temperature gradient is applied to the NRED system as shown in Fig. 7a–c, both the cation and anion flow rates induced by thermophoresis decrease with the increment of the negative temperature gradient. As for the ion flow rates induced by migration at a given negative temperature gradient, the one of cation is enhanced because of the increased temperature but the one of anion is restrained because of the increased potential induced at the right terminal of the reservoir. Therefore, the cation and the anion flow rates induced by migration vary differently with the temperature gradient. In other words, the negative temperature gradient enhances separation of the cations from the anions. Both the cation and anion flow rates induced by diffusion rise with the increment of the negative temperature gradient because of the gradually increased cation and anion diffusivities from the high-concentration side to the low-concentration side. The cation and anion flow rates induced by convection remain unchanged. Finally, the cation transfer number is achieved as an incremental function of the negative temperature gradient by coupling all the factors above. Similarly, when a positive temperature gradient is applied to the NRED system as shown in Fig. 7d–f, both the cation and anion flow rates induced by thermophoresis are enhanced by increasing the positive temperature gradient. Therefore, the separation occurring between the cations and anions is relatively weakened. Variation of cation and anion flow rates induced by migration and convection with the positive temperature gradient are insignificant as for the case of positive temperature gradient. Since both cation and anion diffusivities are gradually decreased from the low-concentration side to the high-concentration side due to the gradually reduced temperature, the ion diffusion from the low-concentration side to the high-concentration side becomes increasingly difficult. Therefore, both the cation and anion flow rates induced by the diffusion decrease with the increment of the positive temperature. The cation transfer number is ultimately achieved as a decremental function of the positive temperature gradient by coupling all the above factors. In generally, compared to the positive temperature gradient, the negative temperature gradient separates the cations from the anions more efficiently.

3.2.2 Effect of Nanochannel Shape

Effects of the nanochannel shape on the energy conversion performance of NRED under conditions of $c_H/c_L = 50$ and four typical temperature fields are primarily investigated first as shown in Fig. 8. The open-circuit potentials (Fig. 8a), the maximum powers (Fig. 8c), and the corresponding cation transfer numbers (Fig. 8d) under the condition of $s = 0.06$ (non-straight nanochannel wall) are generally higher than that under conditions of $s = 0$ (straight nanochannel wall) at all four temperature fields. On the contrary, the short-circuit currents (Fig. 8b) under the condition of $s = 0.06$ are slightly lower than that under conditions of $s = 0$ at all four temperature fields. The temperature field has a more pronounced effect on the energy conversion performance compared to the nanochannel shape.

A series of variation trends of the key performance parameters, summarized in Fig. 9 corporately show how the nanochannel shape acting on the energy conversion process of the NRED system thoroughly. The nanochannel wall fluctuates increasingly as the dimensionless amplitude s rises. On the one hand, as shown in Fig. 9a–d, the increasingly fluctuated wall of the nanochannel mainly affects the ion flow rates induced by the diffusion and the convection and has almost no influence on that induced by the migration and thermophoresis at any given temperature fields. Since the magnitude of ion flow rates induced by the convection is remarkably small, the ion diffusion is the predominant contributor to discrepancies of the ion flow rates across various s . The increasing fluctuation in the local radius of the nanochannel leads to a more pronounced overlap of electric double layer and also set more obstacles along the axial direction which eventually restrains the ion diffusion from the high-concentration side to the low-concentration side. Therefore, both the cation and anion overall flow rates achieved at scenario of \tilde{P}_{max} are reduced when increasing the dimensionless amplitude s at all temperature fields. On the other hand, the surface area and

thus the total surface charges of the nanochannel are enlarged accordingly. At the open-circuit situation, relatively more cations are induced to be accumulated at the downstream end of the nanochannel to balance the increased negative surface charges. Therefore, as shown in Fig. 9e,j, the induced open-circuit potentials achieved at both the positive and negative temperature gradients are enhanced with the increment of the dimensionless amplitude s . Based on the impact of s on both anion and cation flow rates, it is evident that the total current, particularly the short-circuit current as shown in Fig. 9f,k, also shows a consistent variation trend with the rising dimensionless amplitude s . Although the induced open-circuit potential and the short-circuit current vary oppositely with the rising s , the maximum power are finally calculated to be slightly enhanced when rising the dimensionless amplitude s for both negative and positive temperature gradients as shown in Fig. 9g,l. When increasing the dimensionless amplitude s at a certain negative or positive temperature gradient, the fluctuation in the local radius of the nanochannel becomes more significant, which thus gives rise to more regions filled with overlapped electric double layer. Consequently, the ion selectivity of the nanochannel is enhanced and thus the corresponding cation transfer number (Fig. 9h,m) and the maximum energy conversion efficiency (Fig. 9i,n) are increased.

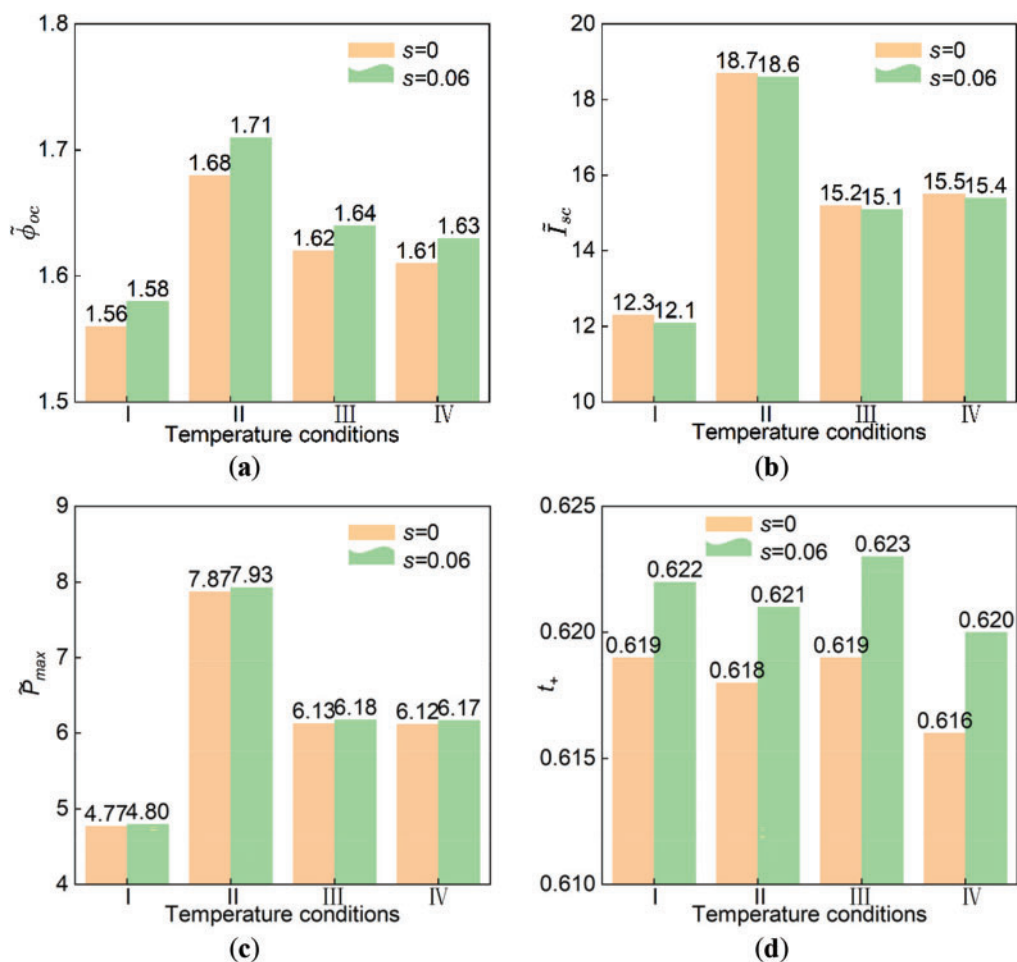


Figure 8: Effects of the nanochannel shape on key performance parameters of the NRED system under condition of $c_H/c_L = 50$ and four different temperature fields. The terms I, II, III, and IV represent temperature fields of $T=298$ K, $T=323$ K, $T=298$ K/323 K, and $T=323$ K/298 K, respectively. (a) Open-circuit voltage, (b) Short-circuit current, (c) Maximum power, and (d) Cation transfer number

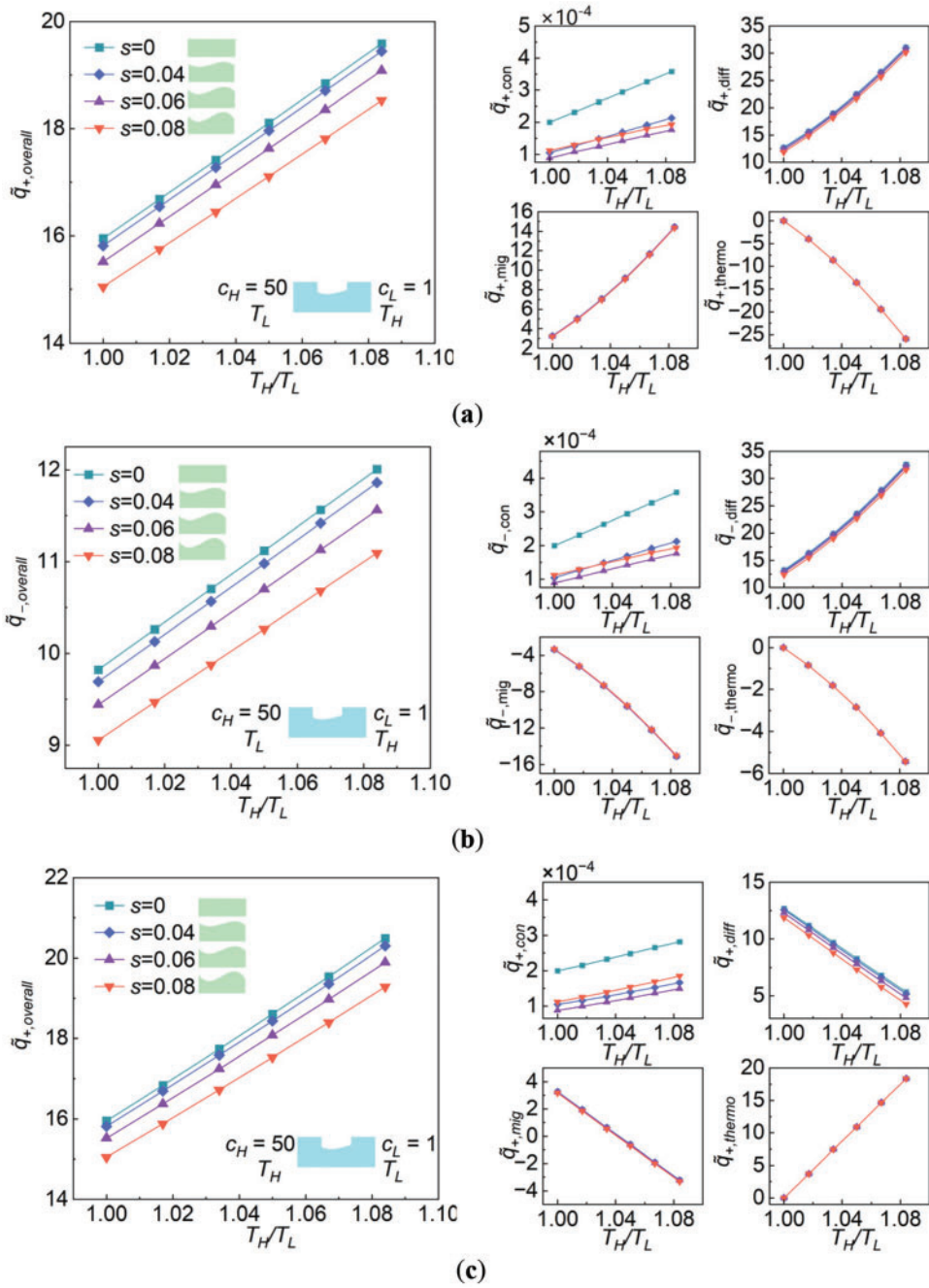


Figure 9: (Continued)

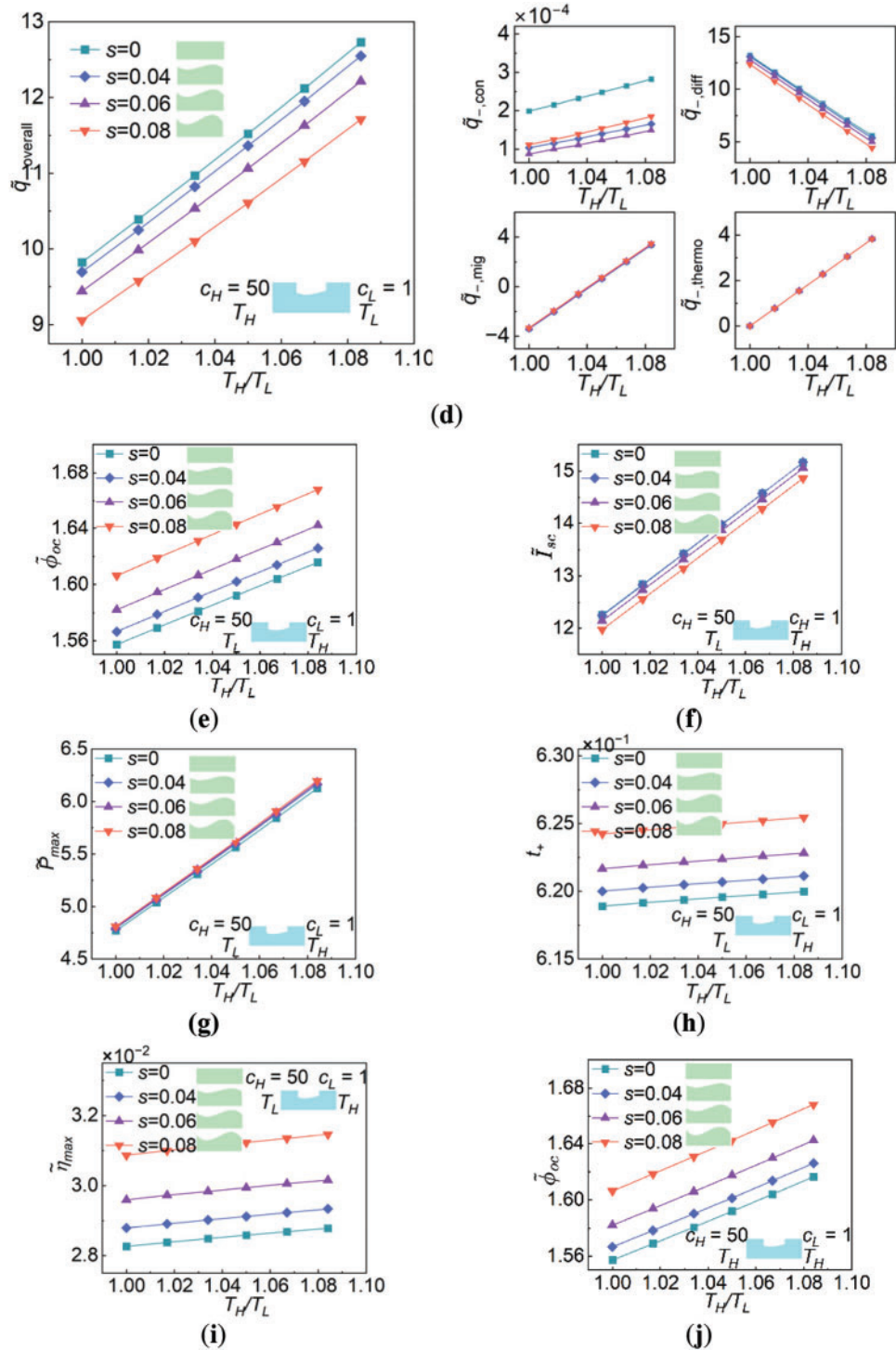


Figure 9: (Continued)

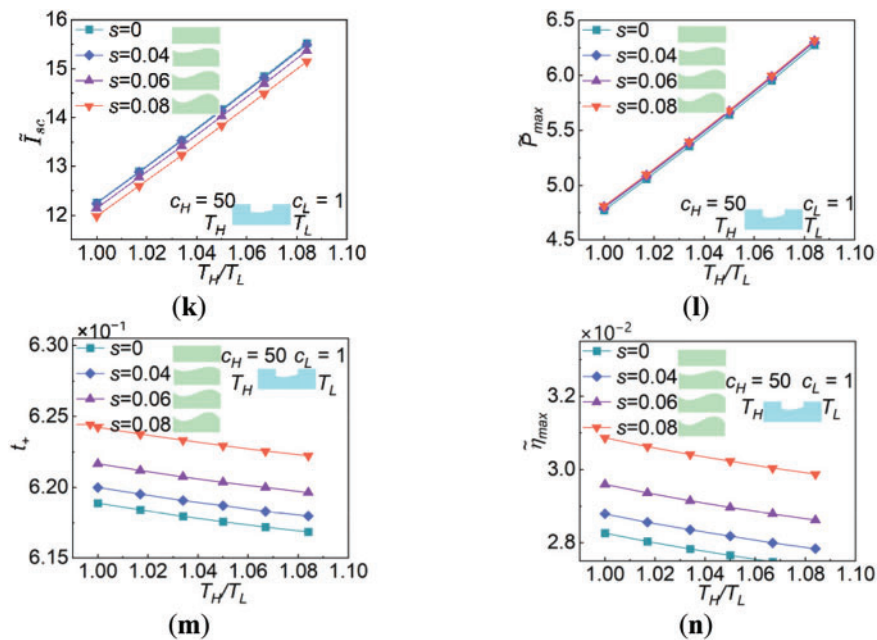


Figure 9: Effects of the nanochannel shape on key performance parameters of the NRED system under condition $c_H/c_L = 50$. (a) Cation flow rates achieved at scenario of \dot{P}_{max} and the negative temperature gradient, (b) Anion flow rates achieved at scenario of \dot{P}_{max} and the negative temperature gradient, (c) Cation flow rates achieved at scenario of \dot{P}_{max} and the positive temperature gradient, (d) Anion flow rates achieved at scenario of \dot{P}_{max} and the positive temperature gradient, (e) Open-circuit potentials at the negative temperature gradient, (f) Short-circuit currents at the negative temperature gradient, (g) Maximum powers at the negative temperature gradient, (h) Cation transfer numbers at the negative gradient, (i) Maximum energy conversion efficiencies at the negative temperature gradient, (j) Open-circuit potentials at the positive temperature gradient, (k) Short-circuit currents at the positive temperature gradient, (l) Maximum powers at the positive temperature gradient, (m) Cation transfer numbers at the positive gradient, (n) Maximum energy conversion efficiencies at the positive temperature gradient

3.2.3 Effect of Concentration

As the source of driven force for ion transportations, the solution concentration plays an important role in determining the energy conversion performance of the NRED system. However, parameters of the energy conversion performance are not always monotonously enhanced by increasing the concentration difference generated between the two terminals of the NRED system.

As shown in Fig. 10a,b, the ion flow rate induced by diffusion at scenario of the maximum power, $s = 0.08$, and $\Delta T = 25$ K, is greatly enhanced by the growth of the concentration gradient compared with the other ones induced by convection, migration, and thermophoresis. This eventually leads to the monotonous variation of the overall current with the concentration gradient as shown in Fig. 10c. Similar trends of the short-circuit currents can also be achieved for different temperature differences at the given condition of $s = 0.08$ (Fig. 10e) and for different dimensionless amplitudes at the given condition of $\Delta T = 25$ K (Fig. 10e).

As for the open-circuit potentials obtained at a relatively large interval of concentration gradient as shown in Fig. 10d,h, they exhibit a slight increase as the concentration ratio rises from 10 to 50, followed by a notable decrease across all varying negative temperature fields (temperature gradient opposite to the concentration gradient) or different dimensionless amplitudes. When the concentration ratio is relatively low, the ion concentration within the NRED system is relatively low which causes the nanochannel being more selective due to the occurrence of the electric double layer. Therefore, a growing number of cations

are attracted by the negatively charged nanochannel to accumulate at the downstream terminal, which leads to the increment of open-circuit potential as rising the concentration ratio from 10 to 50. However, when the concentration ratio continues to increase beyond 50, the electric double layer is gradually screened by free ions within the solution, consequently weakening the ability of the negatively charged surface of the nanochannel to attract more counterions at the downstream terminal. Therefore, the open-circuit potentials decrease significantly as the concentration ratio increases from 50 to 1000.

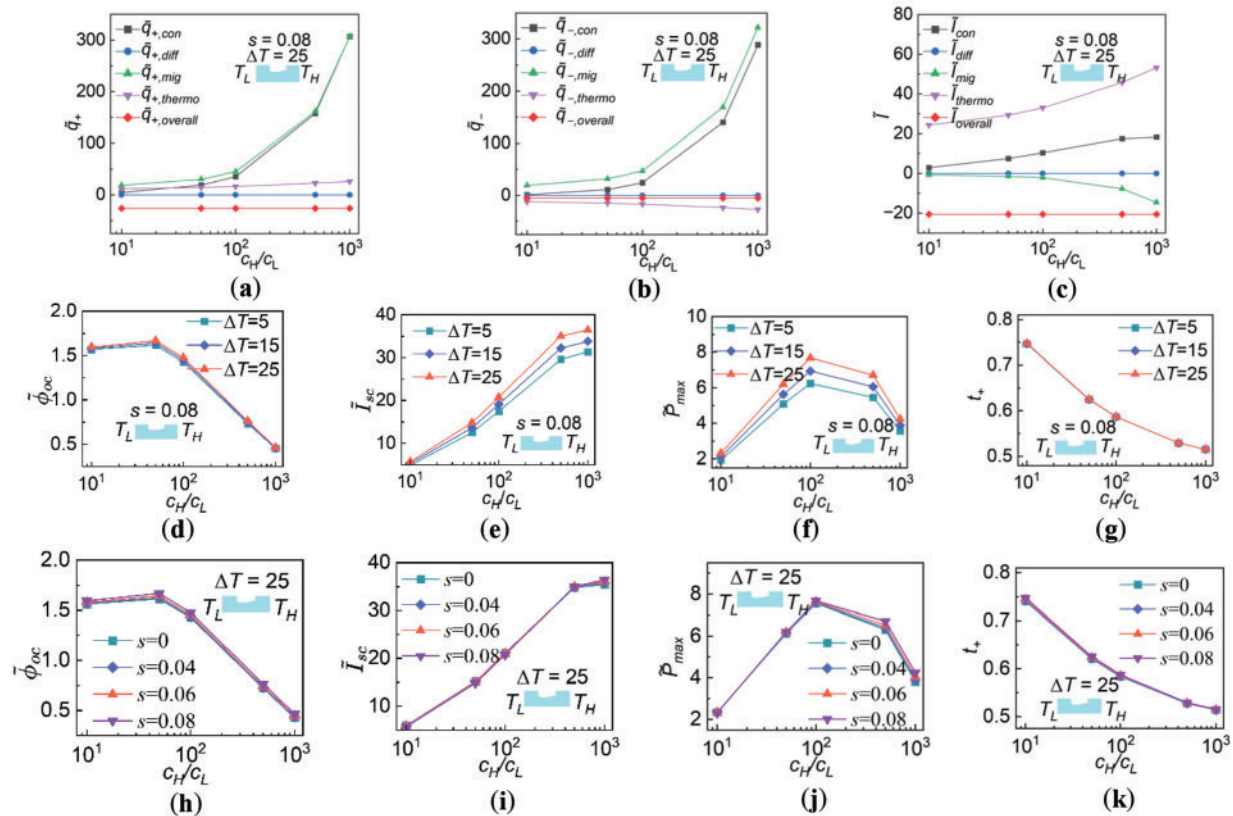


Figure 10: Effects of the concentration on key performance parameters of the NRED system. (a) Cation flow rate at scenario of \tilde{P}_{max} , (b) Anion flow rate at scenario of \tilde{P}_{max} , (c) Current at scenario of \tilde{P}_{max} , (d) Open-circuit potential under condition of $s = 0.08$, (e) Short-circuit current under condition of $s = 0.08$, (f) Maximum power under condition of $s = 0.08$, (g) Cation transfer number under condition of $s = 0.08$, (h) Open-circuit potential under condition of $\Delta T = 25$ K, (i) Short-circuit current under condition of $\Delta T = 25$ K, (j) Maximum power under condition of $\Delta T = 25$ K, (k) Cation transfer number under condition of $\Delta T = 25$ K

The maximum powers are accordingly achieved as shown in Fig. 10f,j. The optimum concentration ratio that giving rise to the highest power happens at the 100 for all varying negative temperature fields or different dimensionless amplitudes. In addition, the high negative temperature gradient can further improve the maximum power due to the enhanced current.

Finally, the progressively elevated solution concentration gradually diminishes the electric double layer, consequently weakening the selectivity of the nanochannel. Therefore, the cation transfer numbers monotonously decrease with the increment of the concentration ratio as shown in Fig. 10g,k.

3.2.4 Multi-Factor Coupling Effects

Different energy conversion performances of NRED can be achieved by varying parameters such as the dimensionless amplitude s , the concentration ratio c_H/c_L , and the temperature difference ΔT , either simultaneously or separately, to investigate their multi-factor coupling effects. The baseline operation conditions are set as $s = 0$, $c_H/c_L = 10$, and $\Delta T = 0$ K. Among all the investigated dimensionless amplitudes in this study, the case of $s = 0.08$ gives the best performance. In addition, the condition where $c_H/c_L = 50$ represents the most prevalent concentration ratio found in natural solution sources, such as the ratio of seawater to river water [8]. Furthermore, high temperature difference at a negative temperature field is found to be able to simultaneously enhance all the performance parameter in this work. Therefore, the target operation conditions of $s = 0.08$, $c_H/c_L = 50$, and $\Delta T = 25$ K at the negative temperature field are applied. Table 2 illustrates the various given conditions and their corresponding performance results.

Table 2: Different energy conversion performances under different given conditions

No.	Given conditions	$\tilde{\phi}_{oc}$	\tilde{I}_{sc}	\tilde{P}_{max}	t_+
Baseline	$s = 0, c_H/c_L = 10, \Delta T = 0$ K	1.532	2.436	1.866	0.739
Case- s	$s = 0.08, c_H/c_L = 10, \Delta T = 0$ K	1.563	2.352	1.837	0.746
Case- c_H/c_L	$s = 0; c_H/c_L = 50, \Delta T = 0$ K	1.557	6.128	4.771	0.619
Case- ΔT	$s = 0.08, c_H/c_L = 50, \Delta T = 25$ K	1.565	2.996	2.345	0.740
Case- $s, c_H/c_L, \Delta T$	$s = 0.08, c_H/c_L = 50, \Delta T = 25$ K	1.668	7.430	6.196	0.625

To elucidate the impacts of varying conditions more clearly, the outcomes of enhancement and impediment are concisely consolidated and illustrated Fig. 11. Changes solely in dimensionless amplitude from 0 to 0.08 or temperature difference from 0 to 25 K result in similar relative variations for each performance parameter, while a change in the concentration ratio alone from 10 to 50 leads to larger relative variations for the short-circuit current and the maximum power. The comparative fluctuations in open-circuit potentials observed under these three distinct conditions exhibit a remarkable similarity. When all condition parameters are changed to the target values of $s = 0.08$, $c_H/c_L = 50$, and $\Delta T = 25$ K, the open-circuit potential, the short-circuit current, and the maximum power are simultaneously enhanced by 8.86%, 204.97%, and 232.01%, respectively. However, the cation transfer number is weakened remarkably by 15.37% under this condition.

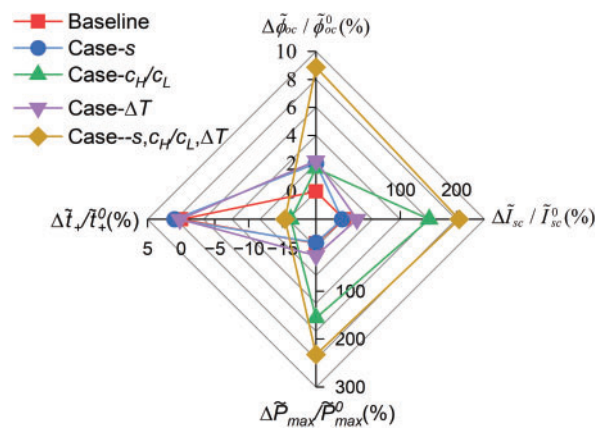


Figure 11: Relative changes in performance parameters at different conditions compared with the baseline condition

4 Conclusions

4.1 Summary and Main Findings

In this comprehensive study, we undertake a numerical investigation into the intricate multi-factorial coupling influences on the energy conversion performance of NRED including the ion flow rate, the open-circuit potential, the short circuit current, the maximum power, and the cation transfer number. Apart from the pivotal parameter of the concentration ratio, we innovatively incorporate a dimensionless amplitude, denoted as s , to emulate the randomly varied wall structure of nanochannels that inherently occur in practical applications, thereby enhancing the realism and applicability of our analysis. The effects of temperature fields in positive and negative gradients on the energy conversion performance are also comprehensively investigated. Finally, we explore the intricate multi-factor coupling effects of nanochannel geometry, concentration ratio, and temperature difference acting on the energy conversion performance of NRED. Generally, this work presents a comprehensive analysis of multi-factor coupling effect of three pivotal operational parameters, including the nanochannel configuration, the temperature field, and the concentration difference, on the energy conversion performance of NRED and thus establishes a robust foundational research base for advancing its industrial utilization prospects. Key findings of this work are concisely summarized as follows.

- (1) At given dimensionless amplitude and concentration field, although the high average temperature of a solution yields better output power, it gives rise to low energy conversion efficiency. Importantly, in contrast to positive temperature gradients that align congruently with the concentration gradient's direction, negative temperature gradients significantly enhance the ion selectivity. This enhancement not only boosts the open-circuit voltage and maximum power but also concurrently elevates the energy conversion efficiency, marking a substantial improvement in the overall performance.
- (2) At given temperature and concentration fields, a nanochannel with large dimensionless amplitude s , indicative of large wall fluctuations, exhibits pronounced enhancements in the open-circuit voltage, maximum power, cation transfer number, and energy conversion efficiency. Notably, while the short-circuit current undergoes a marginal decrement with an increase in this dimensionless amplitude, this subtle reduction does not detract from the overarching improvement observed in the maximum power and corresponding energy conversion efficiency.
- (3) Upon escalating the concentration ratio from 10 to 1000, either within a fixed temperature field or at a constant dimensionless amplitude, the maximum power consistently attains its optimal value at a concentration ratio of 100. Conversely, the cation transfer number experiences a monotonic decrease across this entire range of concentration ratios.
- (4) Upon modifying the operational parameters from the baseline condition of $s = 0$, $c_H/c_L = 10$, and $\Delta T = 0$ K to the targeted condition of $s = 0.08$, $c_H/c_L = 50$, and $\Delta T = 25$ K, there is a concerted improvement observed in the open-circuit potential, short-circuit current, and maximum power, with respective increments of 8.86%, 204.97%, and 232.01%. Notably, despite this overall enhancement, the cation transfer number experiences a notable decrease of 15.37%.

4.2 Limitations and Future Work

While our study offers valuable insights into the multifaceted coupling effects on the energy conversion performance of Nanofluidic Reverse Electrodialysis (NRED), it is important to acknowledge the inherent limitations and assumptions of our model.

Firstly, our model operates under the assumption of steady-state conditions, neglecting the transient effects that are prevalent in real-world systems. In practical applications, NRED systems may undergo

dynamic changes in solution chemistry, temperature gradients, and ion concentrations, all of which can impact performance over time. To address this, future work could incorporate time-dependent simulations to accurately capture these transient phenomena.

Secondly, the nanochannel geometries in our model are idealized, assuming smooth and axisymmetric walls. However, in reality, nanochannels may exhibit surface roughness, irregularities, and non-uniform charge distributions, which can significantly influence ion transport and selectivity. Experimental validation and the development of more sophisticated models that account for these complexities are essential to refine our understanding.

Furthermore, our model simplifies the solution chemistry by focusing solely on KCl solutions. Different salt types and concentrations can alter ionic strength, viscosity, and diffusion coefficients, all of which play a crucial role in energy conversion efficiency. To enhance the applicability of our model, future work should consider a wider range of electrolyte solutions.

Additionally, the effects of temperature on material properties, such as diffusion coefficients and dielectric constants, are currently approximated using empirical relationships. To improve the predictive capability of our simulations, more accurate material models that capture the temperature dependence at the nanoscale should be incorporated.

In conclusion, while our current model provides a solid foundational understanding, there are numerous opportunities to enhance its realism and applicability by addressing the aforementioned limitations. Future research efforts could focus on developing transient simulations, incorporating more realistic nanochannel geometries, expanding the range of electrolyte solutions considered, and refining material property models. These advancements would help bridge the gap between theoretical predictions and the practical implementation of NRED systems.

Acknowledgement: The authors acknowledge Professor Yi Huang from Beihang University for his insightful discussions and invaluable guidance.

Funding Statement: This research was funded by the National Natural Science Foundation of China [52106246] and the Postgraduate Research & Practice innovation Program of Jiangsu Province [KYCX24_1641].

Author Contributions: Conceptualization, Hao Li, Jun Zhang, Hui Wang, Yugang Zhao and Yanmei Jiao; methodology, Hao Li, Yugang Zhao and Yanmei Jiao; software, Cunlu Zhao; validation, Hao Li and Cunlu Zhao; formal analysis, Hao Li, Jinhui Zhou and Yugang Zhao; data curation, Hao Li and Jinhui Zhou; writing—original draft preparation, Hao Li and Jinhui Zhou; writing—review and editing, Jun Zhang, Yugang Zhao and Yanmei Jiao; visualization, Cunlu Zhao, Yugang Zhao and Yanmei Jiao; supervision, Jun Zhang, Hui Wang and Yanmei Jiao; project administration, Jun Zhang and Hui Wang; funding acquisition, Yanmei Jiao. All authors reviewed the results and approved the final version of the manuscript.

Availability of Data and Materials: Not applicable.

Ethics Approval: Not applicable.

Conflicts of Interest: The authors declare no conflicts of interest to report regarding the present study.

References

1. Long R, Kuang Z, Liu Z, Liu W. Reverse electrodialysis in bilayer nanochannels: salinity gradient-driven power generation. *Phys Chem Chem Phys*. 2018;20(10):7295–302. doi:10.1039/C7CP08394G.
2. Mahadeva R, Manik G, Verma OP. Modelling and simulation of desalination process using artificial neural network: a review. *Desalination Water Treat*. 2018;122:351–64. doi:10.5004/dwt.2018.23106.

3. Mei Y, Tang CY. Recent developments and future perspectives of reverse electrodialysis technology: a review. *Desalination*. 2018;425:156–74. doi:10.1016/j.desal.2017.10.021.
4. Tian H, Wang Y, Pei Y, Crittenden JC. Unique applications and improvements of reverse electrodialysis: a review and outlook. *Appl Energy*. 2020;262:114482. doi:10.1016/j.apenergy.2019.114482.
5. Nazif A, Karkhanechi H, Saljoughi E, Mousavi SM, Matsuyama H. Recent progress in membrane development, affecting parameters, and applications of reverse electrodialysis: a review. *J Water Process Eng*. 2022;47(1):102706. doi:10.1016/j.jwpe.2022.102706.
6. Khatibi M, Aminnia A, Ashrafizadeh SN. The role of ionic concentration polarization on the behavior of nanofluidic membranes. *Chem Eng Process-Process Intensif*. 2024;202:109849. doi:10.1016/j.cep.2024.109849.
7. Luca G, Salvo JL, Cipollina A, Luque GL, Fuoco A, Leiva EPM, et al. Vertically aligned carbon nanotubes for monovalent cation selective membranes designed by *in silico* experiments. *Desalination*. 2022;544:116123. doi:10.1016/j.desal.2022.116123.
8. Ma T, Walko M, Lepoitevin M, Janot JM, Balanzat E, Kocer A, et al. Combining light-gated and pH-responsive nanopore based on peg-spiropyran functionalization. *Adv Mater Interfaces*. 2018;5(2):1701051. doi:10.1002/admi.201701051.
9. Balme S, Picaud F, Lepoitevin M, Bechelany M, Balanzat E, Janot JM. Unexpected ionic transport behavior in hydrophobic and uncharged conical nanopores. *Faraday Discuss*. 2018;210:69–85. doi:10.1039/c8fd00008e.
10. Zhang Z, Sui X, Li P, Xie GH, Kong XY, Xiao K, et al. Ultrathin and ion-selective janus membranes for high-performance osmotic energy conversion. *J Am Chem Soc*. 2017;139(26):8905–14. doi:10.1021/jacs.7b02794.
11. Zhang Y, Wu G, Si W, Ma J, Yuan Z, Xie X, et al. Ionic current modulation from DNA translocation through nanopores under high ionic strength and concentration gradients. *Nanoscale*. 2017;9(2):930–9. doi:10.1039/c6nr08123a.
12. Feng J, Graf M, Liu K, Ovchinnikov D, Dumcenco D, Heiranian M, et al. Single-layer MoS₂ nanopores as nanopower generators. *Nature*. 2016;536(7615):197–200. doi:10.1038/nature18593.
13. Hong S, Ming FW, Shi Y, Li RY, Kim IS, Tang CYY, et al. Two-dimensional Ti₃C₂T_x mxene membranes as nanofluidic osmotic power generators. *ACS Nano*. 2019;13(8):8917–25. doi:10.1021/acsnano.9b02579.
14. Yan F, Yao LN, Chen KX, Yang Q, Su B. An ultrathin and highly porous silica nanochannel membrane: toward highly efficient salinity energy conversion. *J Mater Chem A*. 2019;7(5):2385–91. doi:10.1039/c8ta10848j.
15. Zhang Y, Huang Z, He Y, Miao X. Enhancing the efficiency of energy harvesting from salt gradient with ion-selective nanochannel. *Nanotechnology*. 2019;30(29):295402. doi:10.1088/1361-6528/ab0ed8.
16. Jiao Y, Song L, Zhao C, An Y, Lu W, He B, et al. Membrane-based indirect power generation technologies for harvesting salinity gradient energy—a review. *Desalination*. 2022;525:115485. doi:10.1016/j.desal.2021.115485.
17. Yameen B, Ali M, Neumann R, Ensinger W, Knoll W, Azzaroni O. Ionic transport through single solid-state nanopores controlled with thermally nanoactuated macromolecular gates. *Small*. 2009;5(11):1287–91. doi:10.1002/smll.200801318.
18. Guo W, Cao L, Xia J, Nie FQ, Ma W, Xue J, et al. Energy harvesting with single-ion-selective nanopores: a concentration-gradient-driven nanofluidic power source. *Adv Funct Mater*. 2010;20(8):1339–44. doi:10.1002/adfm.200902312.
19. Cao L, Guo W, Ma W, Wang L, Xia F, Wang S, et al. Towards understanding the nanofluidic reverse electrodialysis system: well matched charge selectivity and ionic composition. *Energy Environ Sci*. 2011;4(6):2259. doi:10.1039/c1ee01088c.
20. Kim DK. Numerical study of power generation by reverse electrodialysis in ion-selective nanochannels. *J Mech Sci Technol*. 2011;25(1):5–10. doi:10.1007/s12206-010-1113-x.
21. Long R, Li M, Chen X, Liu Z, Liu W. Synergy analysis for ion selectivity in nanofluidic salinity gradient energy harvesting. *Int J Heat Mass Transf*. 2021;171:121126. doi:10.1016/j.ijheatmasstransfer.2021.121126.
22. Ren Q, Cui Q, Chen K, Xie J, Wang P. Salinity-gradient power harvesting using osmotic energy conversion with designed interfacial nanostructures under thermal modulation. *Desalination*. 2022;535(11):115802. doi:10.1016/j.desal.2022.115802.

23. Hsu JP, Lin SC, Lin CY, Tseng S. Power generation by a ph-regulated conical nanopore through reverse electro dialysis. *J Power Sources*. 2017;366:169–77. doi:10.1016/j.jpowsour.2017.09.022.
24. Kang BD, Kim HJ, Lee MG, Kim DK. Numerical study on energy harvesting from concentration gradient by reverse electro dialysis in anodic alumina nanopores. *Energy*. 2015;86(1):525–38. doi:10.1016/j.energy.2015.04.056.
25. Chein R, Liu B. Energy conversion from electrolyte concentration gradient using charged nano-pores. *Int J Green Energy*. 2016;13(13):1400–11. doi:10.1080/15435075.2016.1206900.
26. Yeh HC, Chang CC, Yang RJ. Reverse electro dialysis in conical-shaped nanopores: salinity gradient-driven power generation. *RSC Adv*. 2014;4(6):2705–14. doi:10.1039/C3RA45392H.
27. Li C, Liu Z, Wang Y, Ali A, Tian ZQ. Energy harvesting from charged conical nanopore with salinity and temperature gradient. *Int J Heat Mass Transf*. 2023;200:123509. doi:10.1016/j.ijheatmasstransfer.2022.123509.
28. Laucirica G, Albesa AG, Toimil-Molares ME, Trautmann C, Marmisollé WA, Azzaroni O. Shape matters: enhanced osmotic energy harvesting in bullet-shaped nanochannels. *Nano Energy*. 2020;71:104612. doi:10.1016/j.nanoen.2020.104612.
29. Zhang X, Qu Z, Wang Q, Iqbal M. Geometry design and mechanism analysis of artificial nanoroughness for enhanced osmotic energy conversion. *Energy Convers Manag*. 2022;273(7411):116373. doi:10.1016/j.enconman.2022.116373.
30. Zhang Y. Effect of temperature on water transportation in nanochannel. *Front Heat Mass Transf*. 2017;9:1–4. doi:10.5098/hmt.9.16.
31. Banerjee D, Yu J, Kang SW, Jeon S. Heat transfer measurements for flow of nanofluids in microchannels using temperature nano-sensors. *Front Heat Mass Transf*. 2012;3(1):1–9. doi:10.5098/hmt.v3.1.3004.
32. Long R, Luo Z, Kuang Z, Liu Z, Liu W. Effects of heat transfer and the membrane thermal conductivity on the thermally nanofluidic salinity gradient energy conversion. *Nano Energy*. 2020;67:104284. doi:10.1016/j.nanoen.2019.104284.
33. Karimzadeh M, Khatibi M, Ashrafizadeh SN, Mondal PK. Blue energy generation by the temperature-dependent properties in funnel-shaped soft nanochannels. *Phys Chem Chem Phys*. 2022;24(34):20303–17. doi:10.1039/D2CP01015A.
34. Han J, Ko Y-S, Nam Y, Lee C. Thermally enhanced osmotic power generation from salinity difference. *J Membr Sci*. 2023;672:121451. doi:10.1016/j.memsci.2023.121451.
35. Song D, Li L, Huang C, Wang K. Synergy between ionic thermoelectric conversion and nanofluidic reverse electro dialysis for high power density generation. *Appl Energy*. 2023;334:120681. doi:10.1016/j.apenergy.2023.120681.
36. Zheng DC, Hsu JP. Enhancing the osmotic energy conversion of a nanoporous membrane: influence of pore density, ph, and temperature. *Phys Chem Chem Phys*. 2023;25(8):6089–101. doi:10.1039/D2CP05831F.
37. Qian F, Zhang W, Huang D, Li W, Wang Q, Zhao C. Electrokinetic power generation in conical nanochannels: regulation effects due to conicity. *Phys Chem Chem Phys*. 2020;22(4):2386–98. doi:10.1039/C9CP05317D.
38. Zhang W, Yan H, Wang Q, Zhao C. An extended teorell-meyer-sievers theory for membrane potential under non-isothermal conditions. *J Membr Sci*. 2022;643:120073. doi:10.1016/j.memsci.2021.120073.
39. Jiao K, Yan HL, Qian F, Zhang WY, Li HY, Wang QW, et al. Energy harvesting based on water evaporation-induced electrokinetic streaming potential/current in porous carbonized carrots. *J Power Sources*. 2023;569:233007. doi:10.1016/j.jpowsour.2023.233007.
40. Benneker AM, Klomp J, Lammertink RGH, Wood JA. Influence of temperature gradients on mono and divalent ion transport in electro dialysis at limiting currents. *Desalination*. 2018;443(3):62–9. doi:10.1016/j.desal.2018.05.005.
41. Mai VP, Yang RJ. Boosting power generation from salinity gradient on high-density nanoporous membrane using thermal effect. *Appl Energy*. 2020;274:115294. doi:10.1016/j.apenergy.2020.115294.
42. Zhang X, Zhang X, Qu Z, Pu J, Wang Q. Thermal-enhanced nanofluidic osmotic energy conversion with the interfacial photothermal method. *Appl Energy*. 2022;326(10):120005. doi:10.1016/j.apenergy.2022.120005.
43. Song D, Zhao Z, Zhao C, Wang T, Li L, Wang K, et al. Collaborative optimization of regeneration unit and power generation unit in reverse electro dialysis heat engine for low-grade heat recovery. *Energy Convers Manag*. 2023;295:117614. doi:10.1016/j.enconman.2023.117614.

44. Liu Z, Lu D, Bai Y, Zhang J, Gong M. Energy and exergy analysis of heat to salinity gradient power conversion in reverse electrodialysis heat engine. *Energy Convers Manag.* 2022;252(9):115068. doi:10.1016/j.enconman.2021.115068.
45. Liu Q, Zhu H, Qu Z. Experiment and simulation analyses of GOM based salinity gradient osmotic energy conversion with nonsymmetric photothermal effect. *Energy Convers Manag.* 2023;298(12):117783. doi:10.1016/j.enconman.2023.117783.
46. Cao Y, Dhahad HA, Parikhani T, Anqi AE, Mohamed AM. Thermo-economic evaluation of a combined kalina cycle and humidification-dehumidification (HDH) desalination system integrated with thermoelectric generator and solar pond. *Int J Heat Mass Transf.* 2021;168(8):120844. doi:10.1016/j.ijheatmasstransfer.2020.120844.
47. Wood JA, Benneker AM, Lammertink RGH. Temperature effects on the electrohydrodynamic and electrokinetic behaviour of ion-selective nanochannels. *J Phys-Condens Matter.* 2016;28(11):114002. doi:10.1088/0953-8984/28/11/114002.
48. Hsu J-P, Chen Y-C, Chen Y-M, Tseng S. Influence of temperature and electroosmotic flow on the rectification behavior of conical nanochannels. *J Taiwan Inst Chem Eng.* 2018;93:142–9. doi:10.1016/j.jtice.2018.10.013.
49. Long R, Kuang Z, Liu Z, Liu W. Temperature regulated reverse electrodialysis in charged nanopores. *J Membr Sci.* 2018;561:1–9. doi:10.1016/j.memsci.2018.05.026.
50. Alinezhad A, Khatibi M, Ashrafizadeh SN. Ionic transfer behavior of bipolar nanochannels resembling PNP nanotransistor. *Electrochim Acta.* 2023;460:142625. doi:10.1016/j.electacta.2023.142625.